CHEMISTRY OF MATERIALS

ARTICLE

pubs.acs.org/cm

Tailoring the Mechanism of the Amorphous-to-Crystalline Phase Transition of $PbTiO_3$ via Kinetically Controlled Hydrolysis

Federico A. Rabuffetti and Richard L. Brutchey*

Department of Chemistry, University of Southern California, Los Angeles, California 90089, United States

Supporting Information

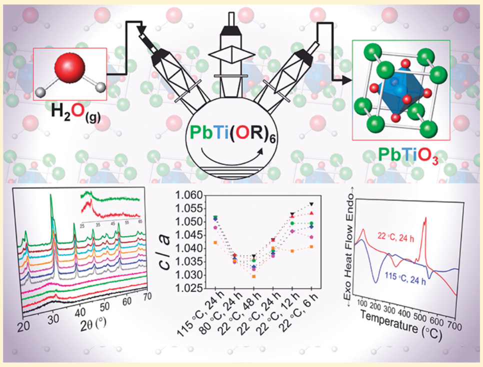

ABSTRACT: A systematic investigation of the effects of hydrolytic conditions on the development of $PbTiO_3$ (PTO) from amorphous metal−organic matrices is reported. Metal−organic matrices were obtained using a novel hydrolytic approach which relies on the kinetically controlled delivery of water vapor at the gas−liquid interface of a Pb−Ti alkoxide precursor. Crystallization was induced via standard thermal treatment and followed using X-ray diffraction, visible Raman spectroscopy, and thermal analysis. It was found that the mechanism of the amorphous-to-crystalline phase transition is controlled by the rate and extent of hydrolysis and polycondensation of the Pb−Ti alkoxide: faster and extended hydrolysis favors an amorphous-to-pyrochlore-to-perovskite transition, whereas slower and less extended hydrolysis favors a direct amorphous-to-perovskite transition. The rate and extent of hydrolysis were found to have a significant impact on the magnitude of the tetragonal distortion of the perovskite unit cell as well. Optimization of hydrolytic conditions allowed for well-crystallized, phase pure, tetragonal PTO to be obtained at temperatures as low as 500 °C via a direct amorphous-to-perovskite phase transition. Differences observed in the mechanism of perovskite phase formation are explained in terms of the differential dependence of the dynamics of lead and titanium atoms on hydrolytic conditions, the former being significantly more affected than the latter. Because long-range redistribution of lead atoms is the rate-determining step of the perovskite phase formation, this finding has implications for the design of metal−organic precursors and hydrolytic approaches targeting the preparation of lead-containing functional perovskite oxides.

KEYWORDS: $PbTiO_3$, vapor diffusion, sol−gel, amorphous, crystalline

INTRODUCTION

Perovskite oxides display a wide variety of technologically important properties such as piezoelectricity, ferroelectricity, and pyroelectricity. $PbTiO_3$ (PTO) is one of the most representative and prominent members of this class of functional materials. At room temperature, its crystal structure is described by the noncentrosymmetric, tetragonal space group *P4mm* ($c/a \approx 1.06$). As a result, it displays large electromechanical coupling factors, large spontaneous polarization, and a high pyroelectric coefficient, making this material an attractive candidate for incorporation into piezo- and pyroelectric transducers and high-energy density capacitors.[1] Furthermore, PTO is one of the end series members of the $Pb(Zr,Ti)O_3$ (PZT) solid solution, which is one of the most widely employed electroceramics.

Complex oxide-based electronic applications require materials with well-defined chemical composition, structure, and functionality in both bulk and thin film form. To this end, numerous soft-chemistry approaches targeting the synthesis of functional perovskite oxides have been developed in the past 25 years. Particularly relevant among these developments is the sol−gel chemistry first proposed by Blum and Gurkovich for the preparation of bulk PTO,[2] and later extended by Budd and coworkers to the preparation of PZT thin films.[3] Since then, sol−gel has become the most widespread approach to technologically relevant electroceramics. This approach starts with the hydrolysis and polycondensation of a heterometallic Pb−(Zr,Ti) alkoxide or a mixture or homometallic alkoxides; a stable colloidal suspension or an amorphous gelatinous precipitate is thus obtained depending on the chemical nature of the precursors. Whether deposited on a substrate or as free-standing powder, these metal−organic matrices are then subjected to thermal treatment in order to induce crystallization of the perovskite phase.

The macroscopic aspects of perovskite phase development from amorphous metal−organic matrices obtained via sol−gel have been extensively studied. As a result, general agreement exists concerning the existence of a metastable fluorite- or pyrochlore-type phase which mediates the amorphous-to-perovskite phase transition.[2,4−14] Because this phase is paraelectric rather than ferroelectric, its presence is detrimental to the functionality of the final product and should be avoided. Unfortunately, complete conversion into the perovskite phase requires extended thermal treatment at temperatures above 500 °C, which in turns causes stoichiometric deviations due to the volatilization of lead. Control of the lead stoichiometry in the final product is achieved by employing ∼10 to 15 mol % excess of

Received: June 27, 2011
Revised: July 25, 2011
Published: August 15, 2011

dx.doi.org/10.1021/cm2018289 | Chem. Mater. 2011, 23, 4063–4076

lead in the precursor solution or,[15] alternatively, by conducting the thermal treatment in a PbO-rich atmosphere.[10,16] From this perspective, achieving a direct amorphous-to-perovskite phase transition that yields well-crystallized, phase pure perovskite upon low-temperature and short thermal treatment is a desirable goal.

Relevant toward this goal is to achieve an atomic-level understanding of the mechanism of the amorphous-to-perovskite phase transition. Although general agreement exists regarding its macroscopic aspects, a comprehensive atomic-level picture is yet to be accomplished. Within that effort, numerous investigators have assessed the influence of the chemical nature of the alkoxide precursor,[15−20] and of hydrolytic[21−27] and thermal treatment[8,15−17,24] conditions on the morphology, local structure, and phase development of amorphous metal−organic matrices. Regarding hydrolytic conditions, it should be noted that hydrolysis of the alkoxide precursor has been invariably carried out via direct hydrolysis, that is, direct liquid−liquid contact between water and the alkoxide. This hydrolytic approach offers poor control over the rate and extent of hydrolysis and polycondensation and ultimately leads to rapid and uncontrolled precipitation. Because of the important role of hydrolysis and polycondensation in sol−gel chemistry, our group has developed a novel hydrolytic approach that relies on the kinetically controlled delivery of water vapor at the gas−liquid interface of a heterometallic alkoxide.[28−30] In contrast to direct hydrolysis, water vapor diffusion offers a high degree of kinetic control over the rate and extent of hydrolysis and polycondensation of the alkoxide precursor; specifically, it circumvents the problem of uncontrolled precipitation, thereby leading to higher chemical homogeneity of the final product. Because of this high degree of kinetic control, vapor diffusion is ideal to investigate the effects of hydrolytic conditions on the phase development of the amorphous metal−organic matrices.

In this work, vapor diffusion was employed to systematically investigate the effect of the rate and extent of hydrolysis of a heterometallic Pb−Ti alkoxide on the development of PTO from amorphous metal−organic matrices. To this end, the alkoxide precursor was hydrolyzed at various temperatures for varying periods of time. Amorphous powders thus obtained were thermally treated to induce crystallization and their phase development was followed by X-ray diffraction, visible Raman spectroscopy, and thermal analysis. The corresponding experimental results are presented and discussed in the context of previous investigations of the local structure and phase development of PTO and PZT from amorphous metal−organic matrices. The implications of these results for the design of metal−organic precursors and hydrolytic approaches targeting the low-temperature synthesis of PTO and PZT are discussed as well.

■ EXPERIMENTAL SECTION

Synthesis of $PbTiO_3$. The synthetic procedure employed in this investigation can be divided into three stages: (1) preparation of the Pb−Ti alkoxide precursor, (2) vapor diffusion, and (3) thermal treatment. In the first two stages, all manipulations were conducted under nitrogen atmosphere using standard Schlenk techniques.

Pb−Ti Alkoxide Precursor. The Pb−Ti alkoxide precursor employed in this work was synthesized using a procedure similar to that described by Kosec and co-workers.[18] Unlike the vast majority of sol−gel routes to PTO that use $Pb(CH_3COO)_2 \cdot 3H_2O$ as the lead source, this procedure uses PbO. The main advantage of this synthetic variation is that it does not require dehydration of the lead precursor to prevent premature hydrolysis and condensation due to the introduction of water during the alkoxide precursor synthesis.[15] PbO (99.999%), $Ti(OCH(CH_3)_2)_4$ (99.999%), and anhydrous 2-methoxyethanol (99.8%) were employed as reagents; all were used as received from Sigma Aldrich. First, 2.872 g (12.87 mmol, 1.000 equivalent) of PbO and 3.80 mL (12.8 mmol, 0.997 equivalent) of $Ti(OCH(CH_3)_2)_4$ were mixed with 20 mL of 2-methoxyethanol in a three-neck round-bottom flask, yielding a yellow suspension. A reflux condenser was attached to the reaction flask and the suspension was heated to 125 °C for 6 h under moderate stirring. The suspension turned into a clear solution after 1 h, indicating the complete dissolution of PbO. The final product consisted of a solution with very light yellow tint and a nominal Pb−Ti concentration of ~0.5 M.

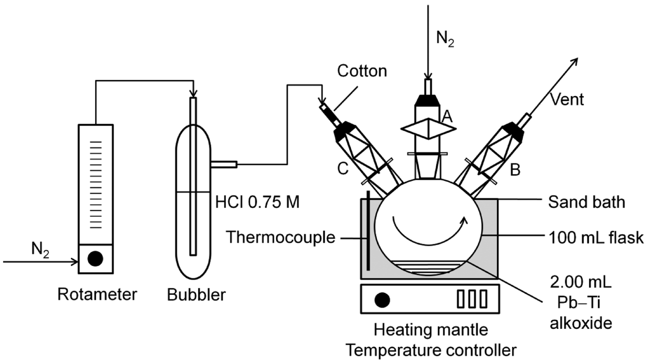

Figure 1. Apparatus employed for the vapor diffusion hydrolysis of the Pb−Ti alkoxide precursor. The apparatus has two operating configurations: (1) precursor injection, in which A is open, B is closed, and a suba septum replaces C; and (2) vapor diffusion, in which stopcock A is closed, and B and C are open. The arrows depict the flow of N_2 gas.

Vapor Diffusion. The apparatus employed for the hydrolysis of the Pb−Ti alkoxide via vapor diffusion is shown in Figure 1. It consists of a 100-mL three-neck flask featuring two gas adapters (A and B) with glass stopcocks; the first connects the reaction flask to the N_2 gas line and the second acts as a vent. In addition, the system features a glass bubbler filled with 50 mL of a 0.75 M HCl solution. The inlet of the bubbler is connected to a needle-valve rotameter, which is in turn connected to the N_2 gas line. The outlet of the bubbler is connected via tygon tubing to a third gas adapter (C) featuring a glass stopcock; this gas adapter allows connection of the bubbler to the reaction flask. The system has two operating configurations: (1) precursor injection (not shown in Figure 1), in which stopcock A is open, B is closed, and a suba septum replaces C; and (2) vapor diffusion, in which stopcock A is closed, and B and C are open, thereby allowing N_2 gas saturated in HCl/H_2O vapor to flow over the alkoxide solution. The vapor flow rate can be controlled via the needle-valve rotameter. The diffusion of vapor over the precursor solution can be carried out at temperatures above ambient by immersing the reaction flask in a heated sand bath.

In this work, the effect of the vapor diffusion temperature (T_{vd}) and time (t_{vd}) on the development of PTO was systematically investigated. For vapor diffusion experiments at room temperature (T_{vd} = 22 °C), the system was set for precursor injection (A open, B closed, and a suba septum replacing C) at the beginning of the each synthetic procedure. Then, 2.00 mL of the Pb−Ti alkoxide were transferred via syringe to the reaction flask. Simultaneously, N_2 was bubbled through the 0.75 M HCl solution. After 30 min of vigorous bubbling, the bubbler was connected to the reaction flask by quickly replacing the suba septum with gas adapter C and the system configuration was switched to vapor diffusion (A closed, and B and C open). An increase in the viscosity of the solution was observed upon continuous flow of vapor. After a certain period of time, referred to as the gelation time hereafter, a fully rigid, monolithic,

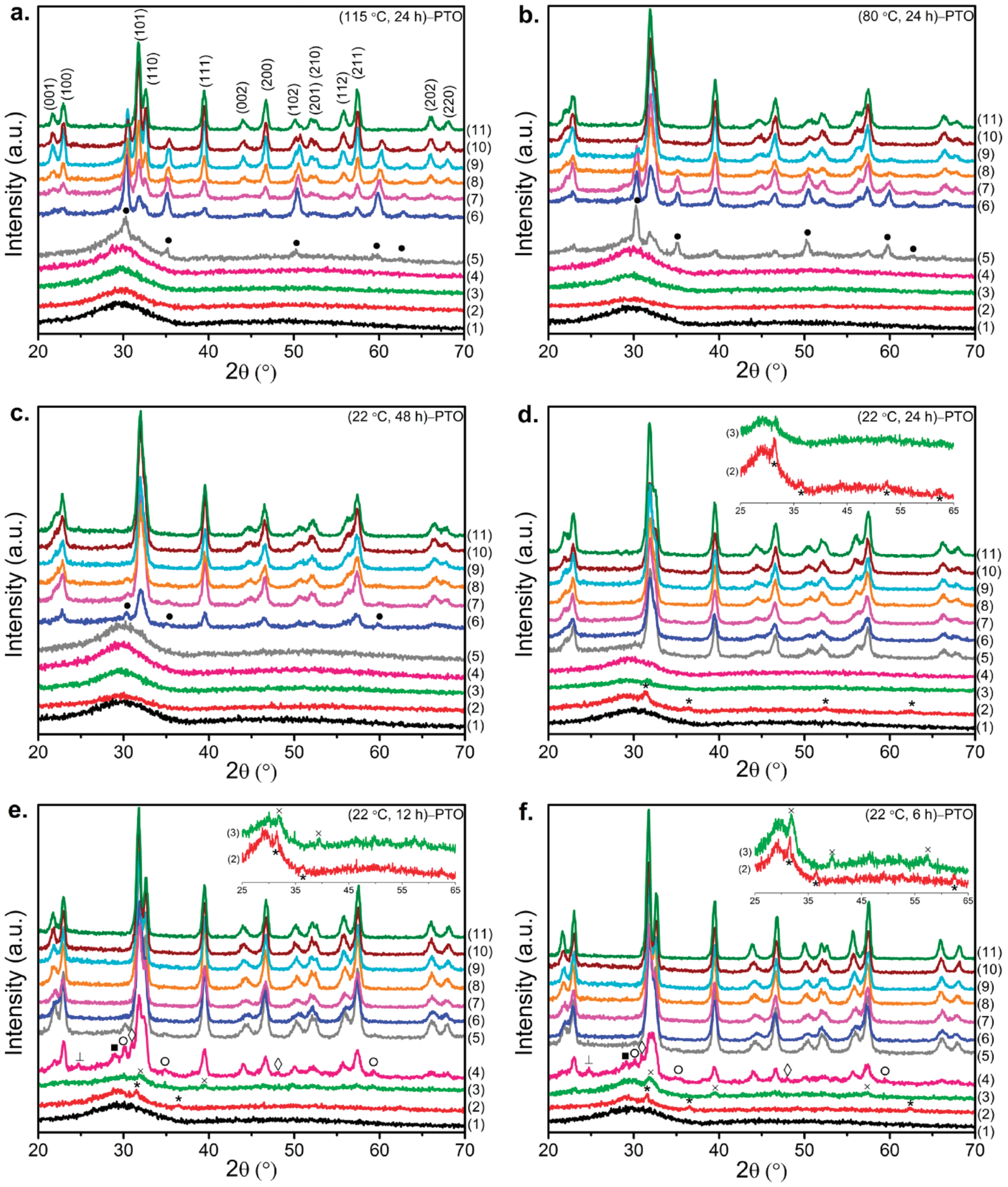

Figure 2. XRD patterns showing the phase development of (T_{vd}, t_{vd})−PTO powders upon thermal treatment. Vapor diffusion conditions are indicated for each sample. Patterns are numbered according to the thermal treatment conditions employed: (1) as-prepared; (2) 400 °C, 0.25 h; (3) 400 °C, 3 h; (4) 450 °C, 0.25 h; (5) 450 °C, 3 h; (6) 500 °C, 0.25 h; (7) 500 °C, 3 h; (8) 600 °C, 0.25 h; (9) 600 °C, 3 h; (10) 700 °C, 0.25 h; and (11) 700 °C, 3 h. Diffraction maxima corresponding to phases other than PTO are denoted by the following symbols: ●, $Pb_2Ti_2O_{7-\delta}$ pyrochlore-type; ★, Pb; ■, PbO; ⊥, $PbCO_3$; ○, lead-deficient pyrochlore-type; ▲ unknown phase(s) (see text for details). Insets: detailed view of selected diffraction patterns; peaks corresponding to PTO are denoted by the × symbol.

and crack-free gel was obtained. The N_2 flow rate was adjusted to obtain gelation times of ∼4 h and maintained constant throughout the whole reaction. Continued flow of vapor resulted in the appearance of a clear supernatant and, eventually, slight cracks in the gel. No precipitation or turbidity was observed at any point of the process. Vapor was allowed to flow over the Pb−Ti alkoxide for a total time t_{vd} (6, 12, 24, or 48 h), which included the gelation time. Then, vapor flow was stopped, the reaction flask opened, the gel disrupted with a spatula, and several pieces of the gel collected. These were washed with 5 mL of absolute ethanol, sonicated for 10 min, and centrifuged at 6000 rpm for 25 min; this washing step was repeated three times. The resulting slurry was dried under vacuum at room temperature for 4 h, yielding a fine white powder.

An identical procedure was followed for vapor diffusion experiments above room temperature (T_{vd} = 80 or 115 °C), with the only difference that the reaction flask containing the Pb−Ti alkoxide was heated to the desired temperature before allowing vapor to flow over. Once in contact with the vapor, the solution became a monolithic gel in ∼2 h, with cracks appearing immediately afterward. Vapor diffusion was carried out for a period of 24 h, through which the vapor flow rate and temperature were held constant. A total of six samples was obtained in the vapor diffusion stage; these will be labeled (T_{vd}, t_{vd})−PTO hereafter.

Thermal Treatment. As-prepared (T_{vd}, t_{vd})−PTO powders were subjected to a standard thermal treatment. The effect of the thermal treatment temperature (T_t) and time (t_t) on the development of PTO was systematically investigated. In a typical treatment, 10 mg of (T_{vd}, t_{vd})−PTO powder were loaded into the alumina pan of a thermogravimetric analyzer TA Q50 (TA Instruments). Then, it was heated to temperature T_t (400, 450, 500, 600, or 700 °C) at a linear rate of 10 °C min^{-1}, under a high-purity air flow (80 mL min^{-1}). The temperature was held constant for a certain time t_t (0.25 or 3 h), after which the sample was air-quenched. Powders thus obtained will be labeled (T_{vd}, t_{vd})−PTO−(T_t, t_t) hereafter.

Characterization. Powder X-ray Diffraction (XRD). XRD patterns were collected in the 20−70° 2θ range using a Rigaku Ultima IV diffractometer operated at 44 mA and 40 kV. Cu Kα radiation (λ = 1.5406 Å) was employed. The step size and collection time were 0.025° and 1 s per step, respectively. Diffraction patterns were recorded at 25 °C.

Raman Spectroscopy. Raman spectra were recorded in the 150−1100 cm^{-1} wavenumber range using a Renishaw inVia Raman microscope (Renishaw). 532 nm radiation from a Nd:YAG laser was employed as the excitation source and the power at the sample level was 3 mW. Sulfur and 4-acetamidophenol were employed as frequency standards for calibration of Raman shifts. The absolute accuracy of Raman shifts was estimated to be ±1 cm^{-1}. All spectra were recorded under ambient conditions.

Thermogravimetry (TG). TG analyses were performed using a thermogravimetric analyzer TA Q50 (TA Instruments) under a high-purity air flow (80 mL min^{-1}). Samples were heated from 30 to 700 °C at a linear rate of 10 °C min^{-1}.

Differential Scanning Calorimetry (DSC). DSC analyses were performed using a DSC8000 (Perkin-Elmer) under a high-purity air flow (20 mL min^{-1}). Samples were placed in an alumina pan and heated from 30 to 700 °C at a linear rate of 10 °C min^{-1}.

■ RESULTS

Powder X-ray Diffraction. Phase Development of Amorphous Powders. XRD patterns showing the development of PTO upon thermal treatment of powders obtained after vapor diffusion are displayed in Figure 2. Visual inspection of the patterns allows samples to be divided into two groups: (1) samples derived from thermal treatment of powders obtained after vapor diffusion at 115 and 80 °C for 24 h, and at 22 °C for 48 h (i.e, (115 °C, 24 h)−, (80 °C, 24 h)−, and (22 °C, 48 h)−PTO, respectively); and (2) samples derived from thermal treatment of powders obtained after vapor diffusion at 22 °C for 24, 12, and 6 h (i.e, (22 °C, 24 h)−, (22 °C, 12 h)−, and (22 °C, 6 h)−PTO, respectively). The development of PTO from each group of samples is described below.

For the (115 °C, 24 h)−, (80 °C, 24 h)−, and (22 °C, 48 h)−PTO samples, the absence of diffraction maxima in the patterns of the as-prepared powders reveals their amorphous character (see pattern (1), Figure 2a−c). Thermal treatment results in the development of long-range order, as indicated by the presence of diffraction maxima. The onset temperatures and times of this amorphous-to-crystalline transition are 450 °C and 3 h for (115 °C, 24 h)− and (80 °C, 24 h)−PTO, and 500 °C and 0.25 h for (22 °C, 48 h)−PTO. Diffraction maxima at 30.4, 35.2, 50.2, 60.3, and 62.5° are observed in the pattern of (115 °C, 24 h)−PTO−(450 °C, 3 h) (see pattern (5), Figure 2a). Both their position and intensity distribution match those of a typical fluorite- or pyrochlore-type phase, whose presence is further confirmed by the intense, dark yellow color of the powder. The appearance of fluorite- or pyrochlore-type phases as intermediates in the development of PTO and PZT from amorphous powders has been extensively reported.[2,4−14,31] These intermediate phases have been shown to be structurally related: indeed, the pyrochlore-type phase is usually formulated as $Pb_2Ti_2O_{7-\delta}$ ($0 \leq \delta \leq 1$) and can be described as a cation-ordered, oxygen-vacant, fluorite-type structure.[8,9,14] Because experimental data presented in this work does not allow the exact structural arrangement of this phase to be identified, these two structures will be treated interchangeably. A second group of diffraction maxima arising from tetragonal PTO (PDF No. 70−4258, space group *P4mm*) appears upon thermal treatment of (115 °C, 24 h)−PTO at 500 °C for 0.25 h (see pattern (6), Figure 2a), thereby allowing for the estimation of the onset temperature and time required for the formation of the perovskite phase. Although both pyrochlore-type and perovskite phases coexist, increasing the thermal treatment temperature and time causes the intensity of the diffraction maxima arising from latter to increase relative to that of the former (see patterns (7)−(10), Figure 2a), resulting in phase pure PTO after treatment at 700 °C for 3 h (see pattern (11), Figure 2a). The progression of this pyrochlore-to-perovskite phase transformation was further confirmed by a gradual change in the color of the samples, which turned from an intense, dark yellow color to the light yellow color typical of the perovskite phase. XRD patterns corresponding to samples derived from thermally treating (80 °C, 24 h)− and (22 °C, 48 h)−PTO powders demonstrate that these undergo a similar amorphous-to-pyrochlore-to-perovskite phase transition upon increasing the temperature and time of the thermal treatment (see Figures 2b and c, respectively). It should be noticed, however, that thermal treatment of (115 °C, 24 h)−PTO at 500 °C for 0.25 h is required to obtain PTO as a minor phase, while a similar result can be obtained by thermally treating (80 °C, 24 h)−PTO at 450 °C for 3 h (see pattern (5), Figure 2b). More importantly, thermal treatment of (22 °C, 48 h)−PTO at 500 °C for 0.25 h yields PTO as the major phase (see pattern (6), Figure 2c). Likewise, thermal treatment of (115 °C, 24 h)−PTO at 700 °C for 3 h is required to obtain phase pure PTO, whereas the same result can be achieved by thermally treating (80 °C, 24 h)−PTO at 700 °C for 0.25 h, or (22 °C, 48 h)−PTO at 600 °C for 3 h. These observations indicate that lowering the vapor diffusion temperature enhances the kinetics of perovskite phase formation.

The as-prepared (22 °C, 24 h)−, (22 °C, 12 h)−, and (22 °C, 6 h)−PTO samples appear amorphous by XRD (see pattern (1), Figure 2d−f). Interestingly, the development of long-range order is observed after thermal treatment at temperatures as low as 400 °C and times as short as 0.25 h (see pattern (2), Figure 2d−f). For all three samples, diffraction maxima with variable intensity are observed at 31.4, 36.5, 52.4, and 63.0° after thermal treatment at 400 °C for 0.25 h; these match the reflections of elemental lead (PDF No. 04−0686) and indicate that a minor amount of Pb^{2+} is undergoing reduction to Pb^0. The partitioning of elemental lead has been reported in previous investigations of the phase development of PTO and PZT from amorphous powders derived via direct hydrolysis of heterometallic alkoxides.[12,32,33] On the basis of the studies of Mantese et al.,[34] Polli and co-workers ascribed the reduction of Pb^{2+} to the low local partial oxygen pressure caused by the decomposition of carbonaceous material.[12]

Extending the thermal treatment from 0.25 to 3 h while keeping the temperature at 400 °C causes the intensity of maxima corresponding to Pb^0 to decrease and eventually vanish (see pattern (3), Figure 2d−f). Simultaneously, weak diffraction maxima arising from PTO become noticeable in the patterns of powders derived from (22 °C, 12 h)− and (22 °C, 6 h)−PTO (see pattern (3), Figure 2e and f, respectively). Interestingly, no intermediate phases are observed during this process; although the possibility these form cannot be ruled out, it is clear they are

Table 1. Effect of Vapor Diffusion and Thermal Treatment Conditions on the Development of $PbTiO_3$[a,b,c]

thermal treatment		vapor diffusion					
T (°C)	t (h)	115 °C, 24 h	80 °C, 24 h	22 °C, 48 h	22 °C, 24 h	22 °C, 12 h	22 °C, 6 h
400	0.25	Am	Am	Am	Am, Pb	Am, Pb	Am, Pb
	3	Am	Am	Am	Am, Pb	Am, PTO	Am, PTO
450	0.25	Am	Am	Am	Am	PTO, Py2, U, PbO, PCO, Am	PTO, Py2, U, PbO, PCO, Am
	3	Am, Py1	Py1, PTO, Am	Am	PTO	PTO, Py2	PTO
500	0.25	Py1, PTO	PTO, Py1	PTO, Py1	PTO	PTO	PTO
	3	Py1, PTO	PTO, Py1	PTO, Py1	PTO	PTO	PTO
600	0.25	PTO, Py1	PTO, Py1	PTO, Py1	PTO	PTO	PTO
	3	PTO, Py1	PTO, Py1	PTO	PTO	PTO	PTO
700	0.25	PTO, Py1	PTO	PTO	PTO	PTO	PTO
	3	PTO	PTO	PTO	PTO	PTO	PTO

[a] Abbreviations: Am, amorphous; PTO, tetragonal $PbTiO_3$; Py1, $Pb_2Ti_2O_{7-\delta}$ pyrochlore-type phase; Py2, lead-deficient pyrochlore-type phase; U, unknown; PbO, orthorhombic PbO; PCO, orthorhombic $PbCO_3$. [b] Major phase is listed first. [c] Dark and light shading depict phase space regions in which tetragonal PTO is observed in conjunction with secondary phases or phase pure, respectively.

not kinetically stable to be detected under these conditions. This observation suggests that a direct amorphous-to-perovskite phase transition preceded by minor lead partitioning is occurring in these samples. Wilkinson et al. observed a similar phase transition during the development of bulk PTO prepared via direct hydrolysis; however, these authors did not provide any rationale for the selection of the hydrolytic conditions which prevented the formation of intermediate pyrochlore-type phases.[9] It should be noted that the diffraction maxima corresponding to PTO are significantly more intense in the pattern of the powder derived from (22 °C, 6 h)−PTO than in that of the powder derived from (22 °C, 12 h)−PTO, implying that decreasing the vapor diffusion time enhances the kinetics of perovskite phase formation.

Increasing the thermal treatment temperature from 400 to 450 °C while keeping the time at 0.25 h has different effects on the phase development of (22 °C, 24 h)−, (22 °C, 12 h)−, and (22 °C, 6 h)−PTO. The pattern corresponding to (22 °C, 24 h)−PTO−(450 °C, 0.25 h) does not display any diffraction maximum besides the broad one resulting from the amorphous matrix (see pattern (4), Figure 2d). In contrast, the patterns of (22 °C, 12 h)−PTO− and (22 °C, 6 h)−PTO−(450 °C, 0.25 h) display several maxima that can be divided into three groups (see pattern (4), Figure 2e and f, respectively). The first group consists of well-defined maxima arising from PTO, which appears as the major phase. The second group includes four weak maxima located at 24.7, 29.0, 31.0, and 48.2°; their reduced number and weak intensity makes assignment rather difficult. Raman data (vide infra) demonstrate the presence of PbO and $PbCO_3$ in these samples. Indeed, the diffraction maxima at 29.0 and 24.7° are in good agreement with the most intense reflection of orthorhombic PbO (PDF No. 72−0093) and $PbCO_3$ (PDF No. 70−2052). The formation of PbO during the development of PTO and PZT from amorphous powders has been extensively reported.[12,14,32,33] Polli et al. observed the formation of PbO following partitioning of elemental lead, and suggested the oxidation of previously formed Pb^0 to Pb^{2+} may be occurring.[12] $PbCO_3$, in turn, likely arises from the reaction of PbO with CO_2 evolved during the combustion of the organic matrix. Diffraction maxima located at 31.0 and 48.2° cannot be assigned at present. Finally, there is a third group of maxima located at 30.1, 34.9, 48.0, and 59.4°, whose position and intensity distribution match those of a pyrochlore-type phase. Interestingly, these maxima appear at lower angles than those corresponding to the pyrochlore-type phase observed after thermal treatment of (115 °C, 24 h)−, (80 °C, 24 h)−, and (22 °C, 48 h)−PTO powders. Because the formation of PbO is not accompanied by partitioning of titanium into binary Ti_xO_y phases, the pyrochlore-type phase observed in this case must be lead-deficient. The formation of lead-deficient pyrochlore-type phases during the development of PTO and PZT from amorphous powders has been reported previously.[13,14,35,36] The occurrence of lead partitioning into PbO and a lead-deficient pyrochlore-type phase after the formation of the perovskite phase further supports the direct nature of the amorphous-to-perovskite phase transition in samples (22 °C, 12 h)− and (22 °C, 6 h)−PTO.

Extending the thermal treatment time from 0.25 to 3 h while keeping the temperature at 450 °C yields phase pure PTO for samples derived from (22 °C, 24 h)− and (22 °C, 6 h)−PTO (see pattern (5), Figures 2d and f, respectively). In contrast, a minor amount of the pyrochlore-type phase is still observed in the pattern corresponding to the sample derived from (22 °C, 12 h)−PTO (see pattern (5), Figure 2e). Noteworthy is the phase development of (22 °C, 24 h)−PTO, which undergoes an amorphous-to-perovskite phase transition in which no intermediate phases are detected; a similar phase development pattern was observed in the same time window for (22 °C, 12 h)− and (22 °C, 6 h)−PTO treated at 400 °C. Therefore, this observation further supports a direct amorphous-to-perovskite phase transition preceded by minor lead partitioning as the mechanism for PTO development

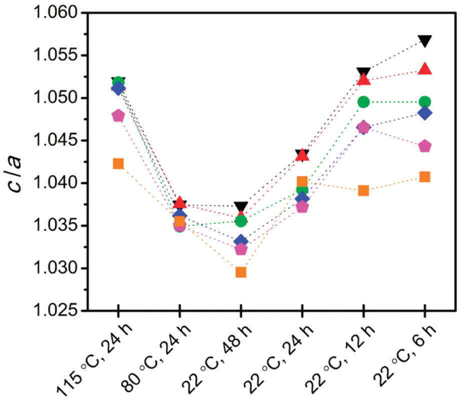

Figure 3. Tetragonal distortion (*c*/*a*) of the PTO unit cell as a function of vapor diffusion conditions. Thermal treatment conditions are indicated according to: orange square, 500 °C, 0.25 h; pink pentagon, 500 °C, 3 h; blue diamond, 600 °C, 0.25 h; green circle, 600 °C, 3 h; red triangle, 700 °C, 0.25 h; and black triangle, 700 °C, 3 h. Dotted lines are guides for the eye.

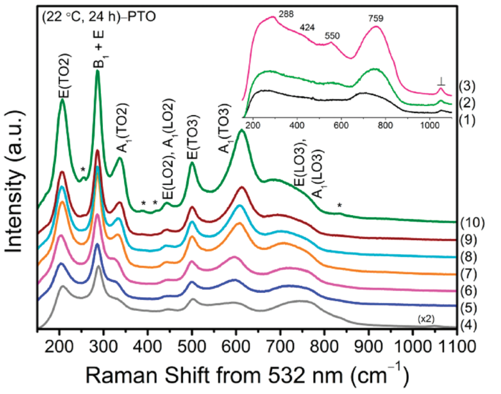

Figure 4. Raman spectra showing the phase development of (22 °C, 24 h)−PTO upon thermal treatment. Spectra are numbered according to the thermal treatment conditions employed: (1) as-prepared; (2) 400 °C, 3 h; (3) 450 °C, 0.25 h; (4) 450 °C, 3 h; (5) 500 °C, 0.25 h; (6) 500 °C, 3 h; (7) 600 °C, 0.25 h; (8) 600 °C, 3 h; (9) 700 °C, 0.25 h; and (10) 700 °C, 3 h. Spectra (1), (2), and (3) are shown in the inset for clarity. Collection of the spectrum corresponding to the sample thermally treated at 400 °C for 0.25 h resulted in strong fluorescence signal. Bands arising from vibrational modes of tetragonal PTO are labeled, whereas bands corresponding to $PbCO_3$ and unknown phases are denoted by ⊥ and ★ symbols, respectively.

from this group of samples. Likewise, it further demonstrates that decreasing the vapor diffusion time enhances the kinetics of perovskite phase formation.

Finally, thermal treatment at 500 °C for 0.25 h results in phase pure PTO (see pattern (6), Figure 2d−f); no other crystalline phases are observed for thermal treatments conducted at higher temperatures and longer times. Although initial partitioning of lead occurs, a well-behaved tetragonal perovskite PTO phase is obtained in all cases, indicating that significant losses of lead do not occur. It should be mentioned the preparation of phase pure PTO was attempted via direct hydrolysis and via direct thermal treatment of the nonhydrolyzed alkoxide precursor. In both cases, thermal treatment at temperatures above 500 °C and times larger than 3 h were required to produce phase pure PTO (see the Supporting Information). The effects of vapor diffusion and thermal treatment conditions on the phase development of amorphous powders are summarized in Table 1.

Structural Aspects. Visual inspection of the diffraction maxima corresponding to the perovskite phase shows these become more intense and narrow upon increasing the thermal treatment temperature and time, regardless of the vapor diffusion conditions employed. Additionally, the splitting of the diffraction maxima resulting from the tetragonal distortion of the perovskite unit cell becomes more noticeable. Both trends demonstrate that for a given set of vapor diffusion conditions, a simultaneous increase in the average crystalline domain size and in the tetragonal distortion of the perovskite unit cell occurs upon thermal treatment.

In this work, however, emphasis is placed on the assessment of the effects of vapor diffusion conditions on the crystal structure of the perovskite phase. Because the splitting of the diffraction maxima is a direct assessment of the magnitude of the tetragonal distortion of the perovskite unit cell (i.e., *c*/*a* ratio) it provides a meaningful metric. In this work, the *c*/*a* ratio was estimated by fitting the two most intense maxima of PTO, namely (101) and (110), with two pseudo-Voight profile functions; the corresponding results are given in Figure 3 for samples thermally treated between 500 and 700 °C. The *c*/*a* ratio varies between ∼1.03 and 1.06. Samples derived from amorphous powders obtained using the same vapor diffusion conditions, exhibit *c*/*a* ratios that behave reasonably well, increasing upon increasing the thermal treatment temperature and time. In the case of samples derived from amorphous powders using different vapor diffusion temperatures and times, the effect of each variable will be analyzed independently of each other. Comparison of (115 °C, 24 h)−, (80 °C, 24 h)−, and (22 °C, 24 h)−PTO shows that decreasing the vapor diffusion temperature results first in a significant decrease and then in a moderate increase of the *c*/*a* ratio. As for the effect of time, comparison of (22 °C, 48 h)−, (22 °C, 24 h)−, (22 °C, 12 h)−, and (22 °C, 6 h)−PTO demonstrates that decreasing the time leads to a gradual increase in the tetragonal distortion. Comparison of *c*/*a* values for (80 °C, 24 h)− and (22 °C, 48 h)−PTO allows the combined effect of both variables to be assessed. The plateau observed on going from the former to the latter indicates the effect of lowering the vapor diffusion temperature from 80 to 22 °C (increase in *c*/*a*) is quasi-exactly counterbalanced by the effect of increasing the time from 24 to 48 h (decrease in *c*/*a*). Previous structural studies of single-crystal,[37,38] bulk,[39−43] and thin film[44] PTO have shown the magnitude of the tetragonal distortion of PTO depends on the size of the crystalline domains as well as on the stress these are subjected to. In the case of size effects, it was found that *c*/*a* decreases upon decreasing the size of the crystalline domain, eventually becoming unity for sizes below ∼10 nm.[39,41−43] Regarding stress effects, it is well-established in the sol−gel literature that crystalline grains develop intrinsic stress as a result of the interaction with each other and/or with the amorphous matrix.[45] This interaction is primarily governed by the microstructural features of the matrix (solvent content, porosity, cracking, etc.). Previous studies of the development of PTO from amorphous matrices found that thermally induced crystallization causes partial relaxation of this intrinsic stress via an expansion of the tetragonal unit cell along the polar *c* axis, resulting in an increase of the *c*/*a* ratio.[13,46] This effect has been shown to be qualitatively and quantitatively analogous to a decrease in the compressive stress of the crystallites due to a reduction in the applied hydrostatic pressure.[13,38,40,44,46] On these bases, the increase in the *c*/*a* ratio observed upon thermal treatment of amorphous powders obtained using the same vapor diffusion conditions can be attributed to both the increase of the average crystalline domain size and the release of stress; size effects are likely to be significant only during the first stages of crystallization, when the presence of nanoscale grains is expected. In contrast, variations of the *c*/*a* ratio observed upon changing the vapor diffusion conditions can be ascribed to differences in the intrinsic compressive stress of perovskite grains. More importantly, they suggest the microstructure of the amorphous matrix gradually changes upon altering the vapor diffusion conditions, thereby influencing the development of the perovskite unit cell.

Raman Spectroscopy. Phase Development of Amorphous Powders. Representative Raman spectra illustrating the development of (22 °C, 24 h)−PTO are shown in Figure 4; spectra corresponding to samples obtained using other vapor diffusion conditions are provided in the Supporting Information. The spectrum corresponding to the as-prepared sample consists of a very broad band centered at ~750 cm^{-1} (see spectrum (1), Figure 4). Thermal treatment of the sample at 400 °C for 0.25 h results in a spectrum (not shown in Figure 4) dominated by a strong fluorescence signal; an identical signal was observed in the spectra of powders derived from (22 °C, 12 h)− and (22 °C, 6 h)−PTO. In addition, all three samples exhibited intense black color after thermal treatment at 400 °C for 0.25 h, indicating that fluorescence arises from the incomplete combustion of the organic matrix. In contrast, identical treatment of (115 °C, 24 h)−, (80 °C, 24 h)−, and (22 °C, 48 h)−PTO yielded powders exhibiting a very opaque and light yellow color, and weak fluorescence signal was observed only in the spectrum of the sample derived from (22 °C, 48 h)−PTO. For this group of samples, the combustion of the organic matrix can be considered to be nearly complete after thermal treatment at 400 °C for 0.25 h. Fluorescence is no longer observed upon extending the heating time from 0.25 to 3 h; a spectrum very similar to that of the as-prepared sample is obtained (see spectrum (2), Figure 4). However, an additional weak band centered at ~550 cm^{-1} and a weak peak at 1054 cm^{-1} are now observed. Bands at ~550 and 750 cm^{-1} are typically observed for the transverse (TO) and longitudinal (LO) vibrational modes of the perovskite structure, respectively. Therefore, their presence indicates that a short-range ordered perovskite-type structure may be developing at this point. The peak located at 1054 cm^{-1} is assigned to the symmetric C−O stretch of the carbonate ion in orthorhombic $\mathrm{PbCO_3}$.[47]

Thermal treatment at 450 °C for 0.25 h results in an increase in the intensity of bands at ~550 and 750 cm^{-1} as well as in the appearance of weak bands at ~288 and 424 cm^{-1}. Their presence further confirms the development of an ordered structure whose spatial coherence is not large enough to be detected by XRD (see pattern (4), Figure 2d). Increasing the thermal treatment time from 0.25 to 3 h results in the appearance of well-defined Raman bands centered at ~205, 286, 323, 443, 499, 596, and 726 cm^{-1} (see spectrum (4), Figure 4); these can be assigned to the E(TO2), B_1 + E, A_1(TO2), E(LO2) + A_1(LO2), E(TO3), A_1(TO3), and E(LO3) + A_1(LO3) vibrational modes of tetragonal PTO (space group *P*4*mm*), respectively.[48] No spectral features other than those arising from the perovskite phase are observed at this point. This observation is in good agreement with XRD data reported earlier for this sample and confirms that a well-behaved PTO structure can be obtained after thermal treatment at 450 °C for 3 h (see spectrum (5), Figure 2d).

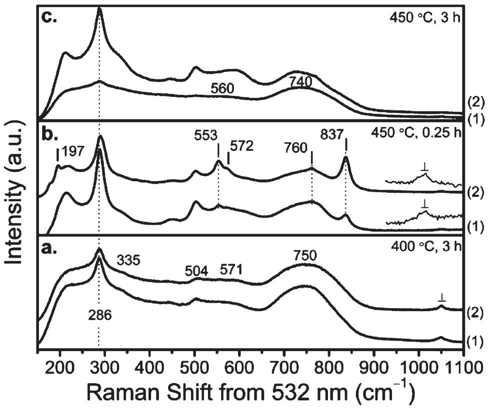

Figure 5. (a) Raman spectra of (1) (22 °C, 12 h)−, and (2) (22 °C, 6 h)−PTO upon thermal treatment at 400 °C for 3 h, respectively. The peak at 1054 cm^{-1} corresponding to $\mathrm{PbCO_3}$ is denoted by the ⊥ symbol. (b) Raman spectra of (1) (22 °C, 12 h)−, and (2) (22 °C, 6 h)−PTO upon thermal treatment at 450 °C for 0.25 h, respectively. Peaks corresponding to phases other than PTO are labeled with the | symbol and their frequencies. The 1000−1100 cm^{-1} region of both spectra is displayed in expanded scale to show the presence of a band at 1054 cm^{-1}. (c) Raman spectra of (1) (115 °C, 24 h)−, and (2) (80 °C, 24 h)−PTO upon thermal treatment at 450 °C for 3 h, respectively.

Further increasing the thermal treatment temperature and time results in an increase in the intensity of the Raman bands and a decrease in their spectral width; both observations are consistent with an increase in the average crystalline domain size. Additionally, a blueshift of the bands arising from E(TO2), A_1(TO2), and A_1(TO3) vibrational modes is observed; the significance of this observation will be discussed in detail later in this section. Finally, weak peaks at ~255, 388, 420, and 835 cm^{-1} appear after thermal treatment at 700 °C for 3 h (see spectrum (10), Figure 4). Similar bands were observed in the spectra of samples derived from (115 °C, 24 h)−, (80 °C, 24 h)−, and (22 °C, 48 h)−PTO after identical thermal treatment. These bands may be due to stoichiometric deviations caused by the volatilization of lead after extended thermal treatment at 700 °C.

Although the above description is representative of the development of PTO from amorphous powders, several other interesting spectral features are observed upon thermal treatment of metal−organic matrices other than (22 °C, 24 h)−PTO, particularly in the 400−450 °C temperature range. Raman spectra of powders derived from (22 °C, 12 h)− and (22 °C, 6 h)−PTO thermally treated at 400 °C for 3 h are given in Figure 5a. Both exhibit bands that are better defined than those observed in the corresponding spectrum of (22 °C, 24 h)−PTO; these are centered at ~286, 335, 504, 571, and 750 cm^{-1}. Noteworthy is the fact that some of these frequencies closely match those of the vibrational modes of tetragonal PTO. This observation is consistent with XRD data reported earlier for these samples and confirms that an amorphous-to-perovskite phase transition occurs upon thermal treatment at 400 °C for 3 h (see pattern (3), Figure 2e,f). Increasing the thermal treatment temperature from 400 to 450 °C and decreasing the time from 3 to 0.25 h results in further development of the bands described above; the corresponding spectra are shown in Figure 5b and both are dominated by bands arising from the perovskite structure. It should be noticed, however, that the peak at 286 cm^{-1} shifts slightly to higher frequencies. Moreover, additional

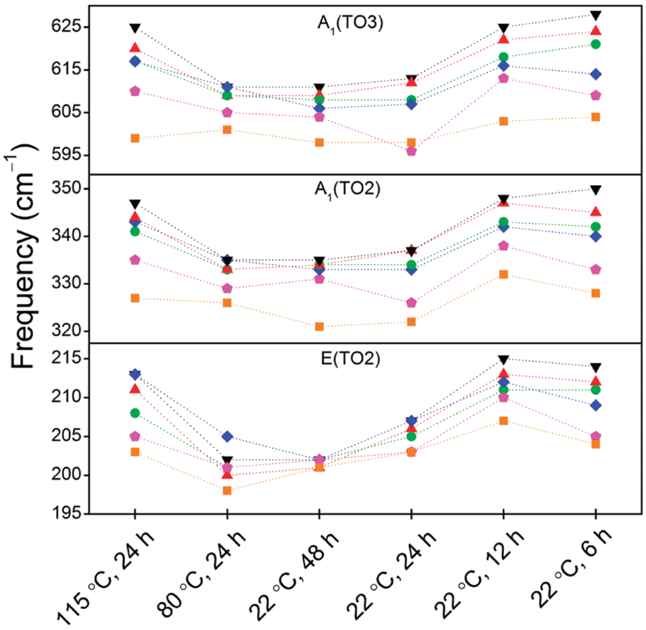

Figure 6. Frequencies of the E(TO2), A$_1$(TO2), and A$_1$(TO3) vibrational modes of PTO as a function of vapor diffusion conditions. Thermal treatment conditions are indicated according to: orange square, 500 °C, 0.25 h; pink pentagon, 500 °C, 3 h; blue diamond, 600 °C, 0.25 h; green circle, 600 °C, 3 h; red triangle, 700 °C, 0.25 h; and black triangle, 700 °C, 3 h. Dotted lines are guides for the eye.

weak and sharp peaks located at 553 and 837 cm^{-1} are observed in the spectrum of (22 °C, 12 h)−PTO−(450 °C, 0.25 h) (see spectrum (1), Figure 5b). Similarly, additional peaks at 197, 553, 572, 760, and 837 cm^{-1} are observed in the spectrum of (22 °C, 6 h)−PTO−(450 °C, 0.25 h) (see spectrum (2), Figure 5b). These additional peaks arise from secondary phases present in these samples. Furthermore, the number and intensity of these additional bands is significantly larger in (22 °C, 6 h)−PTO−(450 °C, 0.25 h), indicating a larger amount of secondary phases relative to the perovskite phase. Both observations are in agreement with XRD data reported earlier for these samples and confirm the amorphous-to-perovskite phase transition is followed by the formation of secondary phases (see spectrum (4), Figures 2e,f). In addition, they confirm the tendency toward larger partitioning upon decreasing the vapor diffusion time. The small blueshift of the 286 cm^{-1} peak and the presence of a weak band at 1054 cm^{-1} are consistent with the presence of PbO and $PbCO_3$, respectively.[47] Regarding the peak at 837 cm^{-1}, it should be mentioned that a similar feature was observed in the spectra of as-prepared (22 °C, 12 h)− and (22 °C, 6 h)−PTO (see the Supporting Information); on this basis, we tentatively assign it to vibrations of residual hydrocarbons present in the powder. Although weak peaks at 197, 553, and 572 cm^{-1} cannot be assigned at present, these are likely to arise from the presence of the lead-deficient pyrochlore-type and unknown phases also present in these samples (see Table 1).

Finally, Raman spectra of powders derived from (115 °C, 24 h)− and (80 °C, 24 h)−PTO thermally treated at 450 °C for 3 h are shown in Figure 5c. The spectrum of (115 °C, 24 h)−PTO−(450 °C, 3 h) appears very similar to that of (22 °C, 24 h)−PTO−(450 °C, 0.25 h) (see spectrum (3), Figure 4), whereas that of (80 °C, 24 h)−PTO−(450 °C, 3 h) appears identical to that of (22 °C, 24 h)−PTO−(450 °C, 3 h) (see spectrum (4), Figure 4). However, the XRD pattern corresponding to (115 °C, 24 h)−PTO−(450 °C, 3 h) shows the presence of a pyrochlore-type phase only (see pattern (5), Figure 2a), whereas that of (22 °C, 24 h)−PTO−(450 °C, 0.25 h) shows no diffraction maxima (see pattern (4), Figure 2d). Likewise, the XRD pattern corresponding to (80 °C, 24 h)−PTO−(450 °C, 3 h) shows a pyrochlore-type phase as the major phase with only a minor amount of the perovskite phase (see pattern (5), Figure 2b), whereas that of (22 °C, 24 h)−PTO−(450 °C, 3 h) only displays maxima corresponding to the perovskite phase (see pattern (5), Figure 2d). The main implication of this observation is that the pyrochlore-type phase observed during the development of (115 °C, 24 h)−, (80 °C, 24 h)−, and (22 °C, 48 h)− PTO is likely to be Raman silent.

Structural Aspects. As mentioned earlier, visual inspection of the spectra depicted in Figure 4 shows that bands arising from E(TO2), A$_1$(TO2), and A$_1$(TO3) vibrational modes of PTO shift to higher frequencies upon increasing the thermal treatment temperature and time. Similar blueshifts were observed in the spectra of powders derived using other vapor diffusion conditions. The frequencies of the E(TO2), A$_1$(TO2), and A$_1$(TO3) vibrational modes are plotted in Figure 6 as a function of the vapor diffusion and thermal treatment conditions. Samples derived from amorphous powders obtained using the same vapor diffusion conditions exhibit vibrational modes whose frequencies increase upon increasing the thermal treatment temperature and time. In the case of samples derived from amorphous powders obtained at different vapor diffusion temperatures and times, the effect of each variable will be analyzed independently of each other. Comparison of (115 °C, 24 h)−, (80 °C, 24 h)−, and (22 °C, 24 h)−PTO shows that decreasing the vapor diffusion temperature results first in a significant decrease and then in a slight increase of the vibrational frequencies. Regarding the effect of vapor diffusion time, comparison of (22 °C, 48 h)−, (22 °C, 24 h)−, (22 °C, 12 h)−, and (22 °C, 6 h)−PTO shows that decreasing the time leads to a gradual increase in the vibrational frequencies. Comparison of vibrational frequencies for (80 °C, 24 h)− and (22 °C, 48 h)−PTO allows the combined effect of both variables to be assessed. The plateau observed on going from the former to the latter indicates the effect of lowering the vapor diffusion temperature from 80 to 22 °C (increase in frequency) is nearly compensated by the effect of increasing the time from 24 to 48 h (decrease in frequency). The variations observed in the vibrational frequencies upon changing the vapor diffusion conditions parallel those observed for the *c*/*a* ratio extracted from XRD data (see Figure 3). In fact, previous investigations of the lattice dynamics of bulk[40,43] and thin film[44] PTO have shown that the frequencies of the E(TO2), A$_1$(TO2), and A$_1$(TO3) vibrational modes and the magnitude of the tetragonal distortion have a similar dependence on size and stress effects. Specifically, these frequencies were found to increase upon increasing the average crystalline domain size or decreasing the hydrostatic pressure on the crystallites, like the polar *c* axis does. Therefore, Raman data can be rationalized in a way similar to the XRD data; that is, the increase in the vibrational frequencies observed upon thermal treatment of amorphous powders obtained using the same vapor diffusion conditions can be ascribed to both an increase of the average crystalline domain size and the relaxation of stress. In contrast, variations observed upon changing the vapor diffusion conditions arise from differences in the intrinsic compressive stress of the perovskite unit cell; these, in turn, reflect changes in microstructure of the amorphous matrices from which PTO develops.

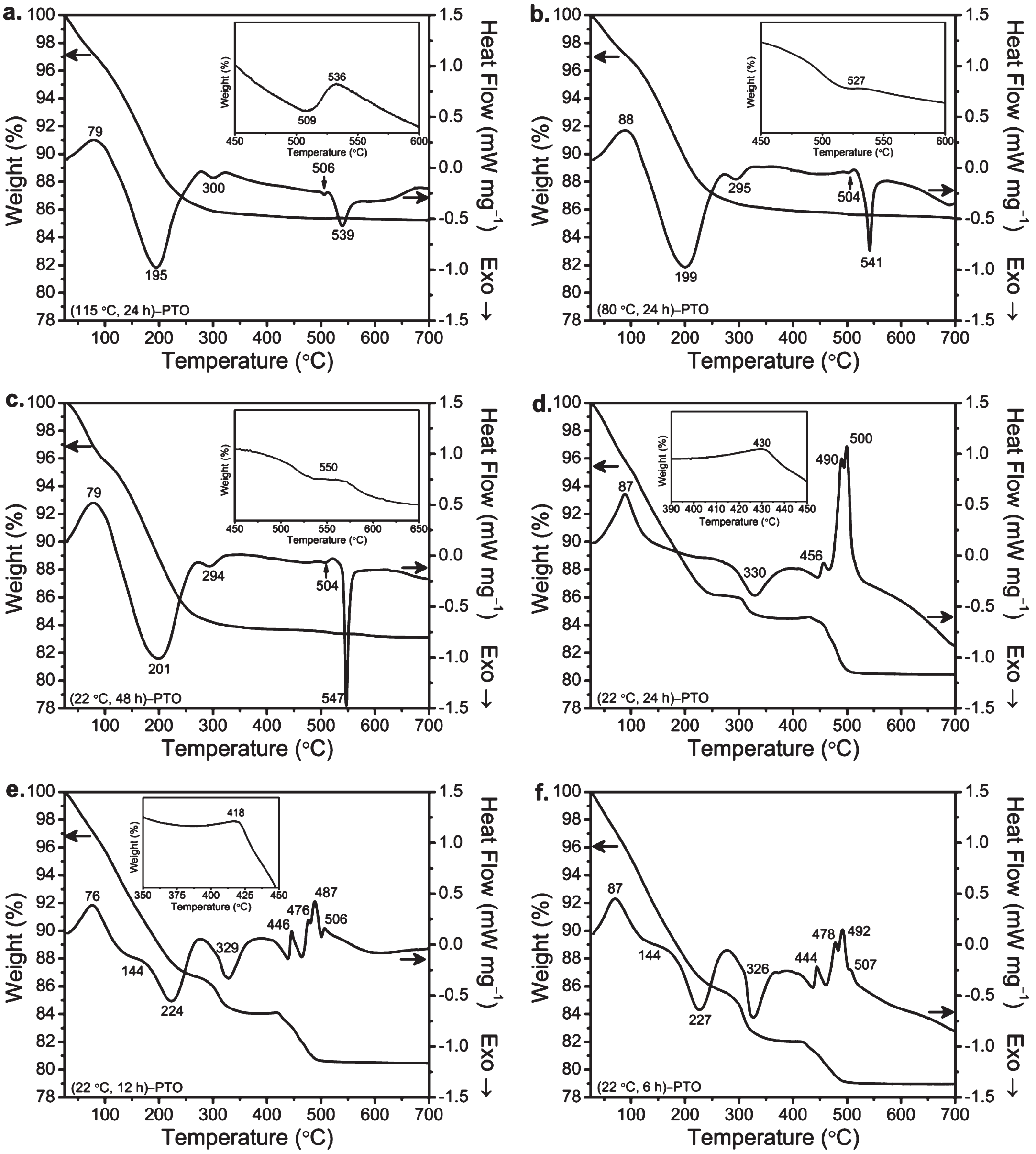

Figure 7. TG and DSC thermograms of as-prepared (T_{vd}, t_{vd})–PTO powders; vapor diffusion conditions are indicated for each sample. Insets: detailed view of selected TG thermograms.

Thermal Analysis. Thermograms from TG and DSC analyses performed on amorphous powders obtained after vapor diffusion are displayed in Figure 7. Similar to what was observed for XRD patterns, visual inspection of the thermograms allows samples to be divided into two groups: (1) (115 °C, 24 h)–, (80 °C, 24 h)–, and (22 °C, 48 h)–PTO; and (2) (22 °C, 24 h)–, (22 °C, 12 h)–, and (22 °C, 6 h)–PTO. The thermal behavior of each group is described below.

TG and DSC thermograms of (115 °C, 24 h)–, (80 °C, 24 h)–, and (22 °C, 48 h)–PTO display little variation upon changing the vapor diffusion conditions (see Figure 7a–c). (115 °C, 24 h)–, (80 °C, 24 h)–, and (22 °C, 48 h)–PTO display total weight losses of ~14.8, 14.4, and 16.9%, respectively. Visual inspection of TG and DSC thermograms shows that weight losses occur in three steps. The first step takes place between 30 and 100 °C and consists of a ~4% weight loss. This loss is accompanied by a broad endothermic peak centered at ~80 °C and is assigned to the removal of water and residual solvents. The second step occurs between 100 and 500 °C and consists of a ~10% weight loss, most of which happens between 100 and 300 °C. This weight loss is accompanied by two broad exothermic peaks centered at ~200 and 300 °C, and is assigned to the combustion of the organic matrix. Raman data reported earlier for these samples demonstrated this process is nearly complete at 400 °C. The third step takes place between 500 and 600 °C and the TG thermograms display a slightly different profile for each sample (see insets, Figure 7a–c). In the case of (115 °C, 24 h)–PTO a very minor weight gain (~0.04 wt %) is observed between 509 and 536 °C, indicating the uptake of oxygen. In contrast, the thermogram of (80 °C, 24 h)–PTO shows little weight loss (~0.20 wt %) with a small plateau centered at 527 °C. A similar plateau is observed in the thermogram of (22 °C, 48 h)–PTO, but in this case it is centered at 550 °C and is rather extended. Interestingly, the corresponding DSC thermograms show very similar profiles in this temperature region, consisting of two exothermic peaks at ~505 and 540 °C; the former is very weak, whereas the second becomes more intense and sharper upon going from (115 °C, 24 h)− to (80 °C, 24 h)− and finally to (22 °C, 48 h)−PTO. XRD data reported earlier demonstrated that an amorphous-to-pyrochlore-to-perovskite phase transition occurs in these samples upon thermal treatment. On that basis, the two exothermic peaks at ~505 and 540 °C are assigned to the crystallization of the pyrochlore-type and perovskite phases, respectively; a similar assignment was proposed in previous investigations of the thermal behavior of amorphous metal−organic matrices derived via direct hydrolysis of Pb−(Zr,Ti) alkoxides.[4,22,49,50] Thermal analysis gives further insight into the nature of the intermediate pyrochlore-type phase. Indeed, oxygen uptake observed in the TG thermogram of (115 °C, 24 h)−PTO but absent in those of (80 °C, 24 h)− and (22 °C, 48 h)−PTO, as well as differences in the extension of the plateau in the TG thermograms of (80 °C, 24 h)− and (22 °C, 48 h)−PTO, suggest the chemical composition, particularly the oxygen deficiency, of the pyrochlore-type phase depend strongly on the vapor diffusion conditions. Finally, no weight losses or heat flow events are observed above 600 °C.

The (22 °C, 24 h)−, (22 °C, 12 h)−, and (22 °C, 6 h)−PTO samples display total weight losses of ~19.5, 19.5, and 21.0%, respectively (see Figures 7d−f). Visual inspection of TG thermograms shows weight losses occur in three steps. The first step takes place between 30 and 280 °C and consists of a ~15% weight loss. This loss is first accompanied by a broad endothermic peak centered at ~80 °C which is assigned to the removal of water and residual solvents. Then, two broad exothermic peaks centered ~145 and 225 °C appear in the DSC thermograms of (22 °C, 12 h)− and (22 °C, 6 h)−PTO; these are assigned to the partial combustion of the organic matrix. The absence of these two peaks in the DSC thermogram of (22 °C, 24 h)−PTO indicates the pyrolytic behavior of the organic matrix changes significantly upon decreasing the vapor diffusion time from 24 to 12 h. The second step occurs between 280 and 375 °C and consists of a weight loss of ~1.5, 2.5, and 3.5% for (22 °C, 24 h)−, (22 °C, 12 h)−, and (22 °C, 6 h)−PTO, respectively. Simultaneously, a broad exothermic peak centered at ~330 °C is observed, and is assigned to the further combustion of the organic matrix. Finally, the third step occurs between 400 and 510 °C and consists of a weight loss of ~4%. Subtle differences are observed upon changing the vapor diffusion time. A very minor weight gain (~0.1 wt %) is noticed for (22 °C, 24 h)− and (22 °C, 12 h)−PTO between 400 and 430 °C and 400 and 416 °C, respectively (see insets, Figures 7d,e), indicating the uptake of oxygen. A similar weight gain was observed by Zimmerman-Chopin and Auer and was assigned to the oxidation of elemental lead formed during partitioning.[22] Indeed, several investigators have suggested that lead present in these metal−organic matrices can undergo a redox process during phase development.[8,12,22,23,32,33,50] The occurrence of redox reactions involving lead would help to explain why well-behaved, tetragonal PTO is obtained despite lead partitioning; that is, why no significant losses of lead occur. The DSC thermogram of (22 °C, 24 h)−PTO features three endothermic peaks at 456, 490, and 500 °C, whereas those of (22 °C, 12 h)− and (22 °C, 6 h)−PTO exhibit four peaks at ~446, 476, 487, and 506 °C. Noteworthy is the fact that the endothermic peaks at 456, 446, and 444 °C in Figure 7d−f, respectively, appear to be located in an exothermic valley. From this description, it is clear that multiple processes take place simultaneously in this temperature window, in agreement with XRD and Raman data reported earlier for this group of samples. These processes include lead partitioning, crystallization of the perovskite phase, and phase transformations of lead-containing phases such as PbO and $PbCO_3$. Additionally, the complete combustion of the organic matrix is achieved in this temperature window. It should be mentioned that thermal treatment of this group of samples at 500 °C for times as short as 5 min resulted in well-crystallized, phase pure PTO, demonstrating that the amorphous-to-perovskite phase transition indeed happens in this temperature window (see the Supporting Information). Finally, no further weight losses or heat flow events are observed above 510 °C.

Comparison of the thermal behavior of these two groups of samples shows that altering the vapor diffusion conditions changes their total weight loss and the pyrolytic behavior of the organic matrix. Regarding weight losses, it is observed these become larger upon decreasing both the vapor diffusion temperature and time; weight losses are ~5 wt % larger for (22 °C, 24 h)−, (22 °C, 12 h)−, and (22 °C, 6 h)−PTO and can be ascribed to a higher carbonaceous content. In terms of the pyrolytic behavior of the organic matrix, similar decomposition patterns are observed for (115 °C, 24 h)−, (80 °C, 24 h)−, and (22 °C, 48 h)−PTO. However, a drastic change takes place upon decreasing the vapor diffusion time from 48 to 24 and then to 12 h, while keeping the temperature at 22 °C. As a result, (22 °C, 24 h)−, (22 °C, 12 h)−, and (22 °C, 6 h)−PTO feature organic matrices whose complete combustion is achieved in the same temperature window where the perovskite phase crystallizes.

Summary. In summary, the most notable findings are:

- A first group of amorphous powders ((115 °C, 24 h)−, (80 °C, 24 h)−, and (22 °C, 48 h)−PTO) undergo a typical amorphous-to-pyrochlore-to-perovskite phase transition upon thermal treatment. For this group of samples, it is observed that lowering the vapor diffusion temperature enhances the kinetics of perovskite phase formation.
- A second group of amorphous powders ((22 °C, 24 h)−, (22 °C, 12 h)−, and (22 °C, 6 h)−PTO) undergo a direct amorphous-to-perovskite phase transition upon thermal treatment. This phase transition is preceded by the formation of elemental lead and followed by the formation Pb^{2+}-containing phases such as $PbCO_3$, PbO, and a lead-deficient pyrochlore-type phase. For this group of samples, it is observed that decreasing the vapor diffusion time enhances both lead partitioning and the kinetics of perovskite phase formation.
- Comparison of the development of PTO from both groups of powders indicates that decreasing both the vapor diffusion temperature and time enhances the kinetics of perovskite phase formation, allowing well-crystallized, phase pure PTO to be obtained after thermal treatment at temperatures as low as 500 °C and times as short as 0.25 h.
- Vapor diffusion conditions have a significant impact on the pyrolytic behavior and microstructure of the metal−organic matrix from which PTO develops. These, in turn, affect the threshold temperature required to achieve its complete combustion, as well as the magnitude of the tetragonal distortion of the perovskite unit cell.

DISCUSSION

Experimental results presented in the previous section demonstrate that the kinetic aspects of the amorphous-to-crystalline phase transition strongly depend on the vapor diffusion temperature and time. Before discussing the implications of this finding, it should be recalled these two experimental variables determine the rate and extent of the hydrolysis and polycondensation of the Pb−Ti alkoxide. The main implication of this consideration is that the mechanism of the amorphous-to-crystalline phase transition is controlled by the extent of hydrolysis and polycondensation of the Pb−Ti alkoxide as well as by the rate at which these two processes occur.

Indeed, our results demonstrate that faster and extended hydrolysis and polycondensation favor an amorphous-to-pyrochlore-to-perovskite phase transition mechanism, whereas slower and less extended hydrolysis and polycondensation favor a direct amorphous-to-perovskite mechanism. Previous investigations of the development of PTO and PZT from amorphous metal−organic matrices have explained the formation of a metastable pyrochlore-type phase in terms of the marginal mobility of Pb^{2+} and Ti^{4+} ions at low to medium temperatures.[9,10,14,16] These diffusional constraints prevent long-range redistribution of species required for the formation of a crystalline structure and limits rearrangements to short and medium ranges, yielding metastable phases with varying degrees of cation ordering. These constraints are relaxed upon increasing the temperature, resulting in the gradual transformation of the pyrochlore-type phase into the highly ordered, thermodynamically stable perovskite phase. From this perspective, the observation of an intermediate pyrochlore-type phase during the crystallization of amorphous powders obtained after fast and extended hydrolysis and polycondensation (i.e., (115 °C, 24 h)−, (80 °C, 24 h)−, and (22 °C, 48 h)−PTO) indicates these have atomic-level structures which restrict long-range redistribution of the Pb^{2+} and Ti^{4+} ions. Likewise, the observation of a direct amorphous-to-perovskite phase transition in samples obtained after slower and less extended hydrolysis and polycondensation (i.e., (22 °C, 24 h)−, (22 °C, 12 h)−, and (22 °C, 6 h)−PTO) suggests their atomic-level structure provides higher mobility and shorter diffusion paths to metal ions. The relaxation of diffusional constraints upon decreasing the rate and extent of hydrolysis and polycondensation is further confirmed by the enhancement of the kinetics of perovskite phase formation observed in both groups of samples upon decreasing the vapor diffusion temperature and time.

Differences in the atomic-level structure of the amorphous matrices are also at the origin of their different partitioning behavior. Thermal treatment of amorphous matrices derived from fast and extended hydrolysis and polycondensation of the Pb−Ti alkoxide, i.e., (115 °C, 24 h)−, (80 °C, 24 h)−, and (22 °C, 48 h)−PTO, results in ternary phases $PbTiO_3$ and $Pb_2Ti_2O_{7-\delta}$. The fact that the Pb:Ti molar ratio in these crystal phases equals unity, as well as the absence of other crystalline phases, indicate that lead and titanium atoms partition equally between the amorphous and crystalline phases. In contrast, thermal treatment of amorphous powders derived from slow and less extended hydrolysis and polycondensation (i.e., (22 °C, 24 h)−, (22 °C, 12 h)−, and (22 °C, 6 h)−PTO) results in partitioning of lead into elemental lead while titanium remains in the amorphous matrix. The subsequent formation of PbO, $PbCO_3$, and a lead-deficient pyrochlore-type phase further confirms this differential partitioning behavior. These differences can be rationalized in terms of the chemical homogeneity of the amorphous matrices. Previous investigations of the molecular structure of Pb−(Zr,Ti) alkoxides have isolated oligomeric structures with 1:2 molar ratios for Pb:Ti, indicating that molecular-level heterogeneity exists in these species.[35,51] It seems reasonable to assume that the likelihood of these oligomeric structures being replicated in the amorphous matrix increases upon decreasing the extent of the hydrolysis and polycondensation of Pb−Ti alkoxide.[24,52,53] Under this assumption, elemental lead partitioning can be explained by considering the formation of isolated, lead-rich domains from unreacted Pb^{2+} ions, as proposed by Polli et al.[12] The stronger tendency for elemental lead partitioning observed upon decreasing the vapor diffusion time can be ascribed to a higher degree of chemical heterogeneity; that is, to more extended lead-rich domains. Likewise, the absence of elemental lead partitioning in amorphous matrices obtained after extended hydrolysis and polycondensation indicates a higher degree of chemical homogeneity. Partitioning of elemental lead was observed by Polli et al. in the course of their investigation of the pyrolytic behavior of amorphous matrices derived via direct hydrolysis of Pb−(Zr,Ti) alkoxides.[12] Although these investigators acknowledged the existence of chemical heterogeneity, they ascribed the formation of elemental lead primarily to the high carbonaceous content of the matrices, which ranged from 15 to 70 wt %. In this work, however, the carbonaceous content of metal−organic matrices in which elemental lead partitioning occurs is only ∼5 wt % larger than that of matrices in which no partitioning is observed. Therefore, it is unlikely that variations in the partitioning behavior of lead can be explained solely on the basis of the carbon content of the amorphous matrices; instead, it is the degree of chemical homogeneity that must be taken into account.

The occurrence of variations in the atomic-level structure of the amorphous metal−organic powders upon changing the hydrolytic conditions is further supported by differences in their pyrolytic behavior. As mentioned earlier, the most remarkable consequence of these variations is that (22 °C, 24 h)−, (22 °C, 12 h)−, and (22 °C, 6 h)−PTO feature organic matrices whose complete combustion is achieved in the same temperature window where the perovskite phase forms. It has been suggested the overlap of these two processes could result in a decrease of the onset temperature required for perovskite phase formation, because the energy released by the combustion of the organic matrix could trigger the nucleation of the perovskite phase even though the external temperature is not high enough.[19,31,33] This effect has been postulated to become more significant upon increasing the carbonaceous content of the metal−organic matrix. In this work, however, the carbonaceous content of metal−organic matrices whose combustion could potentially overlap with the perovskite phase formation is only ∼5 wt % larger than that of matrices in which these two processes are decoupled (i.e., (115 °C, 24 h)−, (80 °C, 24 h)−, and (22 °C, 48 h)−PTO). Furthermore, the significant enhancement of the kinetics of perovskite phase formation observed upon going from (22 °C, 24 h)− to (22 °C, 12 h)− and finally to (22 °C, 6 h)−PTO is accompanied by a very marginal increase in the carbon content of the samples (ca. 1.5 wt %). Therefore, although the coupling between the combustion of the organic matrix and the formation of the perovskite nuclei cannot be ruled out, it is unlikely that variations in the carbonaceous content are at the origin of the enhancement of the kinetics of perovskite phase formation; instead, it is the atomic-level structure of the amorphous matrix that must be considered.

It seems clear at this point that a delicate interplay exists between the degree of hydrolysis and polycondensation of the Pb−Ti alkoxide, the atomic-level structure and partitioning behavior of the metal−organic matrix, and the kinetics of perovskite phase formation. Further insight into this interplay can be gained by considering results from previous investigations of the atomic-level structure of amorphous metal−organic matrices derived from direct hydrolysis of Pb−(Zr,Ti) alkoxides. Of special relevance in the context of this discussion is the work of Sengupta et al., who employed extended X-ray absorption fine structure spectroscopy to characterize the local structure of metal atoms in the amorphous phase.[54] According to these authors, powders derived via hydrolysis of a Pb−Ti alkoxide consist of separate −Pb−O−Pb− and −Ti−O−Ti− networks, rather than a polymeric −Pb−O−Ti− network. Lead atoms were found to exhibit a high degree of disorder, indicating they occupy random positions in the amorphous matrix. In contrast, the local structure around titanium atoms was described as regular TiO_6 polyhedra linked to form a polymeric −Ti−O−Ti− framework with medium-range structural coherence. On the basis of these observations, Sengupta et al. concluded that heterogeneity exists at the atomic-level, and that homometallic rather than heterometallic condensation occurs during the hydrolysis step. Furthermore, they proposed the formation of TiO_6 polyhedra is readily achieved during hydrolysis and low temperature heat treatment. In contrast, formation of PbO_n polyhedra ($n \approx 12$) from lead atoms randomly distributed in the amorphous matrix necessitates further thermal treatment and, therefore, is the rate-limiting step for the formation of the perovskite structure. With slight variations, the structural picture proposed by Sengupta et al. has been shown to hold for amorphous Pb−Ti matrices obtained following using different synthetic routes and processing conditions.[31,55−57]

Reexamination of our experimental results in the context of these findings provides a comprehensive picture of the effects of hydrolytic conditions on the development of PTO from amorphous metal−organic matrices. Starting from the hydrolysis of the Pb−Ti alkoxide, a scenario based on Sengupta's model can be envisaged. In this scenario, homo- rather than heterocondensation occurs regardless of the hydrolytic conditions employed, and the amorphous phase consists of separate −Pb−O−Pb− and −Ti−O−Ti− networks. Decreasing the extent of hydrolysis and polycondensation causes larger chemical heterogeneity, as well as lead atoms to become more loosely packed. Although this results in larger lead partitioning, it also provides lead atoms with enhanced mobility, so their redistribution across domains with different chemical composition is facilitated; this, in turn, favors the direct formation of the perovskite phase. Likewise, more extended hydrolysis and polycondensation results in larger chemical homogeneity and a denser packing of lead atoms. As a consequence, both lead partitioning and mobility are restricted and the formation of a metastable pyrochlore-type phase with varying degrees of cation ordering is kinetically favored. In this scenario chemical heterogeneity exists at the molecular level and, more importantly, hydrolytic conditions have a different effect on the dynamics of lead and titanium atoms: the latter preferentially self-assemble into a polymeric −Ti−O−Ti− framework, whereas the distribution of the former across the amorphous matrix varies significantly. Because this model adequately explains experimental results, differences observed in the mechanism of perovskite phase development from amorphous metal−organic matrices can be ultimately ascribed to the differential dependence of the dynamics of lead and titanium on hydrolytic conditions.

Previous investigations of the phase development of amorphous metal−organic matrices obtained via direct hydrolysis of Pb−(Zr,Ti) alkoxides have overlooked the influence of hydrolytic conditions on the mechanism of perovskite phase formation. These studies have established that the amorphous-to-perovskite phase transition occurs via an intermediate pyrochlore-type phase. Furthermore, agreement exists regarding the use of an excess of lead not only to compensate for PbO losses, but also to promote the crystallization of the perovskite phase. The role of PbO as a "network modifier" of the crystallization dynamics of the perovskite phase was first acknowledged by Polli et al.[14] These investigators observed that increasing the PbO content of the amorphous matrix promotes crystallization of PTO by favoring cation ordering in metastable pyrochlore-type phases. Another outcome of previous investigations is the belief a polymeric −Pb−O−Ti− framework rather than two separated homometallic networks favors the kinetics of perovskite phase formation.[3,12,24] Interestingly, significant differences in the phase development of amorphous metal−organic matrices are observed upon changing the hydrolytic approach from direct to vapor diffusion hydrolysis. Indeed, optimization of vapor diffusion conditions allows for a direct amorphous-to-perovskite phase transition to be achieved, resulting in well-crystallized, phase pure, tetragonal PTO at temperatures as low as 500 °C. Furthermore, this result can be achieved without the use of an excess of lead. In this regard, it should be mentioned that excess of lead is not necessary to produce a significant enhancement of the kinetics of perovskite phase formation as suggested by Polli et al., since the same effect can be achieved via optimization of hydrolytic conditions. Finally, experimental results presented in this work show the perovskite phase can be crystallized directly from two separate −Pb−O−Pb− and −Ti−O−Ti− amorphous networks if lead atoms have a chemical environment that provides them high mobility and short diffusion paths.

These findings have implications for the design of homo- and heterometallic alkoxide precursors employed in soft-chemistry hydrolytic approaches targeting the preparation of PTO and PZT. Important in the context of this discussion is the work of Pradhan et al., who investigated the local structure of metal atoms in amorphous Pb−(Zr,Ti) metal−organic matrices prepared using a nonhydrolytic solvothermal method.[57] These investigators suggested the structure of these matrices must be tailored to have the perovskite structure in a range of ∼1.5 nm in order for a significant enhancement of the crystallization kinetics to occur. Our findings demonstrate that accomplishing this goal requires the chemical environments of lead and titanium atoms in the precursor to be significantly different. Specifically, the chemical environment of lead should be tailored to provide this species with loose packing and maximized mobility, whereas that of the titanium should allow this species to readily self-assemble into TiO_6-type units.

Last, but not least, it should be recalled that hydrolytic conditions not only affect the kinetics of perovskite phase development, but also its crystal structure and lattice dynamics. Specifically, the magnitude of the tetragonal distortion of the perovskite unit cell varies significantly due to microstructural effects on the intrinsic stress of the crystallites. Because the asymmetry of the unit cell is at the origin of the piezo-, ferro-, and pyroelectric properties of PTO, this result further emphasizes the importance of fine control of hydrolytic conditions to achieve a functional material with optimized properties (i.e., maximum c/a ratio).

■ CONCLUSIONS

A novel hydrolytic approach relying on the kinetically controlled delivery of water vapor at the gas−liquid interface of a

Pb—Ti alkoxide precursor was employed to systematically investigate the effects of hydrolytic conditions on the development of PTO from amorphous metal—organic matrices.

It was found the mechanism of the amorphous-to-crystalline phase transition is controlled by the rate and extent of hydrolysis and polycondensation of the Pb—Ti alkoxide. Differences observed in the mechanism of perovskite phase formation were explained in terms of the differential dependence of the dynamics of lead and titanium atoms on hydrolytic conditions: the latter preferentially self-assemble into a polymeric —Ti—O—Ti— framework, whereas the distribution of the former across the amorphous matrix varies significantly. Therefore, fine control over hydrolytic conditions and mobility of lead atoms are critical in the perspective of achieving molecular-level control over the mechanism of the amorphous-to-crystalline phase transition.

Indeed, optimization of hydrolytic conditions allowed for well-crystallized, phase-pure, tetragonal PTO to be obtained at temperatures as low as 500 °C via a direct amorphous-to-perovskite phase transition and without the use of excess of lead. Moreover, vapor diffusion hydrolysis of the alkoxide precursor outperformed direct hydrolysis and direct thermal treatment approaches to PTO, both of which required more severe thermal treatment to accomplish a similar result. Incorporation of these findings into the design of hydrolytic approaches and metal—organic precursors targeting the preparation of technologically relevant electroceramics should help closing the structure-gap existing between the amorphous and crystalline phases.

■ ASSOCIATED CONTENT

Ⓢ **Supporting Information.** The following Supporting Information is provided: (1) XRD patterns of powders obtained after direct hydrolysis of the Pb—Ti alkoxide precursor; (2) XRD patterns of powders obtained after direct thermal treatment of the Pb—Ti alkoxide precursor; (3) Raman spectra showing the phase development of amorphous powders obtained using vapor diffusion temperatures and times other than 22 °C and 24 h, respectively; and (4) XRD pattern of (22 °C, 24 h)—PTO after thermal treatment at 500 °C for 5 min. This material is available free of charge via the Internet at http://pubs.acs.org.

■ AUTHOR INFORMATION

Corresponding Author

*E-mail: brutchey@usc.edu.

■ ACKNOWLEDGMENT

This material is based on work supported by the National Science Foundation under Grant DMR—0906745. The authors are thankful for the generous support provided by the Department of Chemistry and the Dornsife College of Letters, Arts, and Science at University of Southern California. They also thank Prof. Stephen B. Cronin of the Department of Electrical Engineering at University of Southern California for the use of his Raman station. Richard L. Brutchey acknowledges the Research Corporation for Science Advancement for a Cottrell Scholar Award.

■ REFERENCES

(1) Moulson, A. J.; Herbert, J. M. *Electroceramics: Materials, Properties, Applications*; 2nd ed.; John Wiley & Sons: Chichester, U.K., 2003.

(2) Blum, J. B.; Gurkovich, S. R. *J. Mater. Sci.* **1985**, *20*, 4479–4483.

(3) Budd, K. D.; Dey, S. K.; Payne, D. A. *Br. Ceram. Proc.* **1985**, *36*, 107–120.

(4) Selvaraj, U.; Prasadaro, A. V.; Komarneni, S.; Brooks, K.; Kurtz, S. *J. Mater. Res.* **1991**, *7*, 992–996.

(5) Tuttle, B. A.; Headley, T. J.; Bunker, B. C.; Schwartz, R. W.; Zender, T. J.; Hernandez, C. L.; Goodnow, D. C.; Tissot, R. J.; Michael, J. *J. Mater. Res.* **1992**, *7*, 1876–1882.

(6) Kwok, C. K.; Desu, S. B. *Appl. Phys. Lett.* **1992**, *60*, 1430–1432.

(7) Kwok, C. K.; Desu, S. B. *J. Mater. Res.* **1993**, *8*, 339–343.

(8) Brooks, K. G.; Reaney, I. M.; Klissurska, R.; Huang, Y.; Bursill, H. L.; Setter, N. *J. Mater. Res.* **1994**, *9*, 2540–2553.

(9) Wilkinson, A. P.; Speck, J. S.; Cheetham, A. K. *Chem. Mater.* **1994**, *6*, 750–754.

(10) Seifert, A.; Lange, F. F.; Speck, J. S. *J. Mater. Res.* **1995**, *10*, 680–691.

(11) Lakeman, C. D. E.; Xu, Z.; Payne, D. A. *J. Mater. Res.* **1995**, *10*, 2042–2051.

(12) Polli, A. D.; Lange, F. F. *J. Am. Ceram. Soc.* **1995**, *78*, 3401–3404.

(13) Bersani, D.; Lottici, P. P.; Montenero, A.; Pigoni, S.; Gnappi, G. *J. Mater. Sci.* **1996**, *31*, 3153–3157.

(14) Polli, A. D.; Lange, F. F.; Levi, C. G. *J. Am. Ceram. Soc.* **2000**, *83*, 873–871.

(15) Schneller, T.; Waser, R. *J. Sol—Gel Sci. Technol.* **2007**, *42*, 337–352.

(16) Levefre, M. J.; Speck, J. S.; Schwartz, R. W.; Dimos, D.; Lockwood, S. J. *J. Mater. Res.* **1996**, *11*, 2076–2084.

(17) Schwartz, R. W.; Boyle, T. J.; Lockwood, S. J.; Sinclair, M. B.; Dimos, D.; Buchheit, C. D. *Integr. Ferroelectr.* **1995**, *7*, 259–277.

(18) Kosec, M.; Delalut, U.; Malic, B.; Bobnar, V.; Drazic, G. *Proceedings of the Tenth IEEE International Symposium on Applications of Ferroelectrics*; IEEE: Piscataway, NJ, 1996; Vol. 1—2, pp 443—446.

(19) Kwon, Y. T.; Lee, I.-M.; Lee, W. I.; Kim, C. J.; Yoo, I. K. *Mater. Res. Bull.* **1999**, *34*, 749–760.

(20) Malic, B.; Kosec, M.; Arcon, I.; Kodre, A. *J. Sol—Gel Sci. Technol.* **2000**, *19*, 153–156.

(21) Dey, S. K.; Budd, K. D.; Payne, D. A. *J. Am. Ceram. Soc.* **1987**, *70*, C295–C296.

(22) Zimmermann-Chopin, R.; Auer, S. *J. Sol—Gel Sci. Technol.* **1994**, *3*, 101–107.

(23) Zhang, Q.; Vickers, M. E.; Patel, A.; Whatmore, R. W. *J. Sol—Gel Sci. Technol.* **1998**, *11*, 141–152.

(24) Fukui, T. *J. Sol—Gel Sci. Technol.* **1998**, *11*, 31–41.

(25) Ion, E.-D.; Malic, B.; Kosec, M. *J. Eur. Ceram. Soc.* **2007**, *27*, 4349–4352.

(26) Lakeman, C. D. E.; Payne, D. A. *J. Am. Ceram. Soc.* **1992**, *75*, 3091–3096.

(27) Zhang, Q.; Huang, Z.; Vickers, M. E.; Whatmore, R. W. *J. Eur. Ceram. Soc.* **1999**, *19*, 1417–1421.

(28) Brutchey, R. L.; Morse, D. E. *Angew. Chem., Int. Ed.* **2006**, *45*, 6564–6566.

(29) Brutchey, R. L.; Cheng, G. S.; Gu, Q.; Morse, D. E. *Adv. Mater.* **2008**, *20*, 1029–1033.

(30) Beier, C. W.; Cuevas, M. A.; Brutchey, R. L. *J. Mater. Chem.* **2010**, *20*, 5074–5079.

(31) Camargo, E. R.; Longo, E.; Leite, E. R.; Mastellaro, V. *J. Solid State Chem.* **2004**, *177*, 1994–2001.

(32) Li, S.; Condrate, R. A.; Spriggs, R. M. *J. Can. Ceram. Soc.* **1988**, *57*, 61–65.

(33) Bel Hadj Tahar, R.; Bel Hadj Tahar, N.; Ben Salah, A. *J. Cryst. Growth* **2007**, *307*, 40–43.

(34) Mantese, J. V.; Micheli, A. L.; Hamdi, A. H.; West, R. W. *Mater. Res. Bull.* **1989**, *14*, 48–53.

(35) Chae, H. K.; Payne, D. A.; Xu, Z.; Ma, L. *Chem. Mater.* **1994**, *6*, 1589–1592.

(36) Chen, C.; Ryder, D. F.; Spurgeon, W. A. *J. Am. Ceram. Soc.* **1989**, *72*, 1495–1498.

(37) Sanjurjo, J. A.; Lopez-Cruz, E.; Burns, G. *Phys. Rev. B* **1983**, *28*, 7260–7268.

(38) Nelmes, R. J.; Katrusiak, A. *J. Phys. C: Solid State Phys.* **1986**, *19*, L725–L730.

(39) Zhong, W. L.; Jiang, B.; Zhang, P. L.; Ma, J. M.; Cheng, H. M.; Yang, Z. H.; Li, L. X. *J. Phys.: Condens. Matter* **1993**, *5*, 2619–2624.

(40) Meng, J.; Zou, G.; Ciu, Q.; Zhao, Y.; Zhu, Z. *J. Phys.: Condens. Matter* **1994**, *6*, 6543–6548.

(41) Chattopadhyay, S.; Ayyub, P.; Palkar, V. R.; Multani, M. *Phys. Rev. B* **1995**, *52*, 13177–13184.

(42) Ishikawa, K.; Nomura, T.; Okada, N.; Takada, K. *Jpn. J. Appl. Phys.* **1996**, *35*, 5196–5198.

(43) Ma, W.; Zhang, M.; Lu, Z. *Phys. Status Solidi A* **1998**, *166*, 811–815.

(44) Dobal, P. S.; Bhaskar, S.; Majumder, S. B.; Katiyar, R. S. *J. Appl. Phys.* **1999**, *86*, 828–834.

(45) Exarhos, G. J.; Hess, N. J. *Thin Solid Films* **1992**, *220*, 254–260.

(46) Bersani, D.; Lottici, P. P.; Lopez, T.; Ding, X.-Z. *J. Sol—Gel Sci. Technol.* **1998**, *13*, 849–853.

(47) Bouchard, M.; Smith, D. C. *Spectrochim. Acta, Part A* **2003**, *59*, 2247–2266.

(48) Burns, G.; Scott, B. A. *Phys. Rev. B* **1973**, *7*, 3088–3101.

(49) Caruso, R.; de Sanctis, O.; Fratini, A.; Steren, C.; Gil, R. *Surf. Coat. Technol.* **1999**, *122*, 44–50.

(50) Ju, J.; Wang, D.; Lin, J.; Li, G.; Chen, J.; You, L.; Liao, F.; Wu, N.; Huang, H.; Yao, G. *Chem. Mater.* **2003**, *15*, 3530–3536.

(51) Ma, L.; Payne, D. A. *Chem. Mater.* **1994**, *6*, 875–877.

(52) Bradley, D. C.; Gaze, R.; Wardlaw, W. *J. Chem. Soc.* **1957**, 469–478.

(53) Malic, B.; Arcon, I.; Kosec, M.; Kodre, A. *J. Mater. Res.* **1997**, *12*, 2602–2611.

(54) Sengupta, S. S.; Ma, L.; Adler, D. L.; Payne, D. A. *J. Mater. Res.* **1995**, *10*, 1345–1348.

(55) Feth, M. P.; Weber, A.; Merkle, R.; Reinohl, U.; Bertagnolli, H. *J. Sol—Gel Sci. Technol.* **2003**, *27*, 193–204.

(56) Leite, E. R.; Paris, E. C.; Longo, E.; Lanciotti, F.; Campos, C. E. M.; Pizani, P. S.; Mastellaro, V. *J. Am. Ceram. Soc.* **2002**, *85*, 2166–2170.

(57) Pradhan, S. K.; Gateshki, M.; Niederberger, M.; Ren, Y.; Petkov, V. *Phys. Rev. B* **2007**, *76*, 014114.